Development of a library for far-field sonic boom prediction in OpenFOAM

Artem Maslov[1,2][0009−0005−6255−5946] and Andrey Epikhin[1][0000−0002−6249−4283]

[1] Ivannikov Institute for System Programming of the Russian Academy of Sciences, Moscow, Russia
[2] Moscow Institute of Physics and Technology, Dolgoprudny, Russia

Abstract. This paper presents the development and implementation of the OpenFOAM library for far-field sonic boom prediction using quasi-linear Whitham theory. The proposed numerical algorithm differs in the order of application of the area balancing rule, which makes the algorithm easier to implement and debug. The numerical simulations of the Seeb-ALR, 69°-delta wing and c25d aircraft models presented in the first and second sonic boom workshops are performed. The supersonic flow solvers rhoCentralFoam and dbnsFoam from the OpenFOAM software are used to obtain the near-field pressure signatures. To validate the developed library, the far-field pressure is calculated with the OpenFOAM simulation data. The results show good agreement with the experimental data and the simulation results of the workshop participants.

Keywords: Sonic boom · Far-field pressure · Supersonic flow · Quasi-linear Whitham theory · OpenFOAM

1 Introduction

Supersonic flight is characterized by intense noise exposure to the environment, including sonic boom, which can cause damage and adverse effects to biological and anthropogenic objects [5, 19]. As a result, civil supersonic flights were restricted over the surface of most countries. Currently, the problem of developing a new generation of civil supersonic aircraft whose noise on the ground does not exceed the permissible level is relevant again [2, 3]. Researchers are actively working on this problem in the USA, Russia, China, UK and other countries [2, 3, 16, 25]. International sonic boom workshops were organized by NASA [9, 11, 12].

The far-field sonic boom is affected by many physical phenomena. For example, a stratified atmosphere with wind, aircraft manoeuvrers including acceleration, etc. [15, 20, 26]. The noise level at the ground is calculated from the pressure response, which can be obtained in three different ways. The first method is to perform a real flight with pressure measurements on the ground. The main advantage of this method is to obtain a pressure signature that takes into account all the physical effects that occur during the propagation of shock waves in the atmosphere to the ground. Numerical methods can be further validated using

ICCS Camera Ready Version 2025
To cite this paper please use the final published version:
DOI: 10.1007/978-3-031-97570-7_27

the experimental data obtained. The disadvantages are high time and financial costs. It should be noted that a wind tunnel experiment is not possible due to the scale of the problem, as the far field is at a distance of more than a hundred characteristic lengths of the model. The second method is CFD, such as the numerical solution of the Navier-Stokes equations. This method is less expensive than a physical experiment, but it requires a detailed mesh with a large number of cells to accurately resolve shock waves. Modeling the propagation of shock waves to the surface would require a supercomputer with thousands of cores. The third approach is the most widely used. It uses approximate theories to calculate far-field sonic boom. This method is less accurate than CFD, but it allows the computational cost to be significantly reduced. Such approaches include the quasi-linear theory of Whitham [23, 24], the waveform parameter method [20], the theory of Yu.L. Zhilin [8, 26]. These theories are based on the results of geometric acoustics. The difference between these theories and geometric acoustics is the consideration of nonlinear effects that occur during the propagation of shock waves to the ground, which lead to waveform distortions. The paper [8] provides integral formulas that simplify the calculation of a function similar to the Whitham function. The disadvantage of these theories is that the shock rise time is zero. Therefore, quantitative noise level metrics such as PL [18] cannot be used to infer the acceptability of the sonic boom, because the Fourier transform is used to calculate the metric and is not applicable to a function with discontinuities due to the fact that the resulting spectrum will have infinite energy. Another weakness of the theory is the lack of consideration of advanced physical phenomena such as molecular relaxation and thermoviscous adsorption. These physical phenomena are taken into account, for example, in the method based on the solution of differential augmented Burgers equations. This method is implemented in [4, 16, 17]. In contrast to the quasilinear theory, the shock rise time is not corrected by empirical dependencies, but is calculated by solving differential equations. The method allows molecular relaxation and thermoviscous adsorption to be taken into account. In the above papers, the stratified atmosphere with horizontal wind is also considered.

In this paper, the quasi-linear Whitham theory is used because of its simplicity of implementation. However, this theory is sufficient to predict the far field sonic boom to a first approximation. According to the theory, the Whitham function or a similar function describes the evolution of the acoustic noise at any distance from the aircraft. This function depends on the geometric shape of the aircraft. There are several ways to calculate the sonic boom based on the quasilinear theory. The first method is based on the calculation of Whitham function from the shape of the aircraft and is used in the papers [8, 20, 23, 24, 26]. In addition to the calculation of the sonic boom in the far field, this method can be used for the approximate calculation of the near field, which is useful in sonic boom minimization problems where it is necessary to have a fast algorithm for the calculation of the pressure signature for a constantly changing shape of the aircraft. The second method is proposed in the paper [6] for the case of a given near-field pressure field, e.g. from numerical simulation or experiment. In this

ICCS Camera Ready Version 2025
To cite this paper please use the final published version:
DOI: 10.1007/978-3-031-97570-7_27

paper, based on this approach, a numerical algorithm has been developed and implemented using the OpenFOAM open source library[1], since OpenFOAM allows the numerical modeling of various physical problems and has an actively developing user community. Despite the fact that a large number of applications were developed to model the propagation of far-field sound effects: PCBOOM [14], sBOOM [17], bBOOM [16], vBoom [4] and others, the main problem is that they are not open and therefore each research group working on this topic has to develop its own numerical modeling algorithm. A lot of time and resources are spent to develop such programs. Errors can occur in the development of new code and these errors can lead to incorrect results. Therefore, the problem of developing an open source far-field modeling program is relevant. The advantage of open source software is the possibility to check the correctness of the algorithm, to search for errors and to develop the code further by the community.

The paper is organized as follows: equations for the calculation of the far-field pressure signature using Whitham's theory are described in section 2. A correction factor for the real atmosphere, where pressure and temperature vary with altitude, is also given. A detailed description of the numerical algorithm is given in section 3. Issues that may arise during the implementation of the proposed algorithm are discussed in subsection 3.1. Features of the implementation in OpenFOAM are presented in subsection 3.2. The results of far-field sonic boom simulations using the proposed method for the Seeb-ALR, 69°-delta wing and c25d are described in section 4. The obtained near- and far-field pressure signatures are validated against NASA sonic boom workshop data and discrepancies are discussed.

2 Mathematical model of far-field shock waves

Pressure perturbations at a distance r from the point of origin in the homogeneous atmosphere are described by the Whitham function $F(y)$, which is related to the overpressure relative to the undisturbed flow $\frac{\Delta p}{p_a}(x)$ as follows [23, 24]:

$$F(y) = \frac{\sqrt{2\beta r}}{\gamma M^2} \cdot \frac{\Delta p}{p_a}(x), \tag{1}$$

where p_a is the pressure of undisturbed air at the flight altitude, $M = \frac{v}{c}$ is the Mach number, $\gamma = \frac{C_P}{C_V}$ is the ratio of specific heats of air, and the coefficient $\beta = \sqrt{M^2 - 1}$. The relation between the coordinate x and the argument of Whitham function y is defined by the equation:

$$y = x - \beta r + k\sqrt{r} \cdot F(y), \tag{2}$$

where the coefficient k is given by the formula:

$$k = \frac{(\gamma + 1)M^4}{\sqrt{2}\beta^{3/2}}. \tag{3}$$

ICCS Camera Ready Version 2025
To cite this paper please use the final published version:
DOI: 10.1007/978-3-031-97570-7_27

To compute the pressure signature at the ground, the correction for inhomogeneous atmosphere is needed:

$$\Delta p = \Delta p_W \cdot K_p K_g, \tag{4}$$

where Δp_W is the overpressure calculated by Whitham theory using equations (1) and (2), $K_p = \sqrt{\frac{p_g}{p_a}}$ is the rough correction factor for inhomogeneous atmosphere, where pressure and temperature vary with altitude [13], p_g is the pressure at the ground, K_g is the ground reflection factor, which is the amplification of the wave magnitude due to the interference of the ground reflected wave with the incident wave.

3 Numerical algorithm

The Whitham function depends in a complex way on the aircraft geometry. In the case of a known near-field pressure distribution from physical experiment or numerical simulation, Hicks and Mendoza [6] proposed an algorithm to calculate the far-field pressure. From the near-field pressure distribution (Fig. 1a), the Whitham function (Fig. 1b) is found using the formulas (1), (2). In order to evaluate the non-linear shape distortion with the formation of shock waves during propagation to the ground, it is necessary to correct the Whitham function by the area balancing rule. The final far-field pressure signature (Fig. 1d) is then calculated using equations (1), (2) with the modified Whitham function.

The algorithm implemented in this paper differs from the algorithm of Hicks and Mendoza in the order of application of the area balancing rule. In the proposed algorithm, the Whitham function is not modified but used to compute a multivalued coordinate function (Fig. 1c). To eliminate the ambiguity, the shockwaves are placed according to the equal-area rule. This makes the algorithm easier to debug, as it is possible to draw the calculated shocks on the multi-valued pressure distribution and visually check that the cut-off areas to the left and right of the shock are equal. The numerical method proposed by Yu.L. Zhilin [8, 26] calculates a function similar to Whitham's from the geometric shape of the aircraft, whereas in this paper it is calculated from the near-field pressure fields obtained from the OpenFOAM simulation.

A full description of the proposed algorithm is given below to clarify the differences between the discussed algorithms.

1. Calculate Whitham function (Fig. 1b) using equations (1) and (2) from the known near-field pressure signature $\frac{\Delta p}{p_h}(x)$ (Fig. 1a)
2. Calculate multi-valued far-field pressure distribution (Fig. 1c) using the Whitham function by the equations (1) and (2).
3. Place the shocks to obtain the single-valued pressure distribution (Fig. 1d) using the area-balancing technique: the shock is placed so that the areas it cuts off from the pressure signature on the left and right are equal.

ICCS Camera Ready Version 2025
To cite this paper please use the final published version:
DOI: 10.1007/978-3-031-97570-7_27

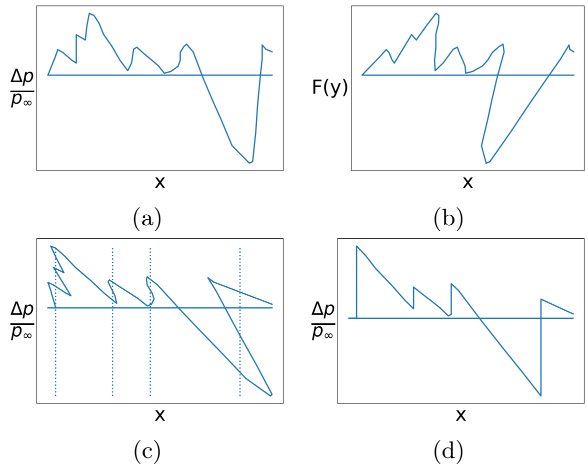

Fig. 1: Far-field pressure prediction algorithm: a) near-field pressure; b) Whitham function; c) multivalued far-field pressure; d) final far-field pressure distribution

3.1 Numerical algorithm for shock waves placement

The pressure distribution is interpolated by a piecewise linear function and considered as a set of points on the plane. To make the algorithm more universal and work for arbitrary pressure signatures, auxiliary points are added. As an example, consider a possible pressure signature (Fig. 2a). After executing the far-field pressure calculation algorithm described in the previous section, the multivalued pressure distribution shown in Figure 2b is obtained. Next, the shockwave placement algorithm is executed using the area-balancing rule. This involves the calculation of the areas cut off from the distribution by vertical lines. For the distribution in the figure 2c this cannot be done for the shock waves shown in red. To solve this problem, auxiliary points (A, B, C) are added and the resulting distribution is shown in the figure 2c.

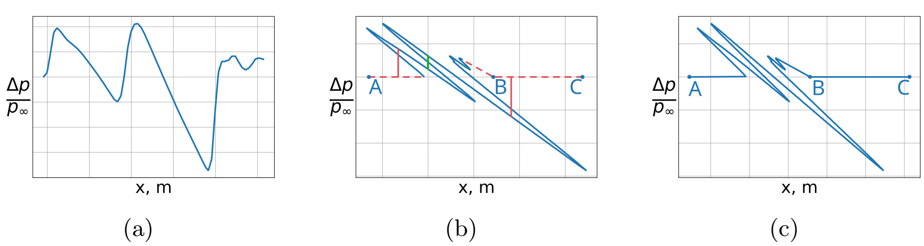

Fig. 2: Auxiliary point addition algorithm: a) near-field; b) far-field without auxiliary points; c) far-field with auxiliary points

ICCS Camera Ready Version 2025
To cite this paper please use the final published version:
DOI: 10.1007/978-3-031-97570-7_27

Auxiliary point B is added by extrapolating the pressure distribution from the right to zero. Later, the coordinates of points A and C will be estimated. The pressure distribution points are denoted as (x_i, p_i), where $i = n, f$ for the near and far fields, respectively. Using the equations (1) and (2) it is possible to obtain the relationship between the coordinates of the near and far fields:

$$x_f = x_n + \beta(r_f - r_n) - k(\sqrt{r_f} - \sqrt{r_n})\frac{\sqrt{2\beta r_n}}{\gamma M^2}p_n. \quad (5)$$

If $p_n = 0$, the points are shifted by $\Delta_0 = \beta(r_f - r_n)$, denoted by $x_0 = x_n + \Delta_0$. If $p_n > 0$, then the point is shifted to the left by $\Delta(p_n) = k(\sqrt{r_f} - \sqrt{r_n})\frac{\sqrt{2\beta r_n}}{\gamma M^2}|p_n| > 0$ relative to x_0, similarly, if $p_n < 0$, it is shifted to the right by $\Delta(p_n)$ relative to x_0. Then the coordinates of the help point A are $(\min x - \Delta(\max p_n), 0)$, those of point C are $(\max(\max x, x_B) + \Delta(\max p_n))$, where x_B is the abscissa of the point B.

As an example, the far-field pressures have the distribution shown in Figure 3. To speed up the algorithm, an array of orientation points 0-11 is created during the first traversal of the pressure distribution points. The first and the last point are always orientation points. The inner point is the orientation point if the distribution line at that point «changes direction» from left to right or vice versa (the line has a right direction if x_i and x_{i+1} are $x_{i+1} > x_i$ for two adjacent points $x_{i+1} > x_i$). Due to the presence of auxiliary points A and C, shock waves must be searched for between odd $2k-1$ and even $2k$ orientation points, $k \in \mathbb{N}$. The shocks between points x_{2k-1} and x_{2k} are searched for using a simple iterative method. The segment $[x_{2k}, x_{2k-1}]$ is divided into N parts. A shock wave is placed at each partition point and the areas cut off from the pressure distribution are calculated. The final position of the shock is the point where the difference in modulus between the right and left regions is the smallest (Fig. 3a). In this situation, the shock waves s_2 and s_4 overlap s_3 and s_5 (Fig. 3a), so, the retarded one are removed. The final unambiguous far-field pressure distribution is shown in figure 3b.

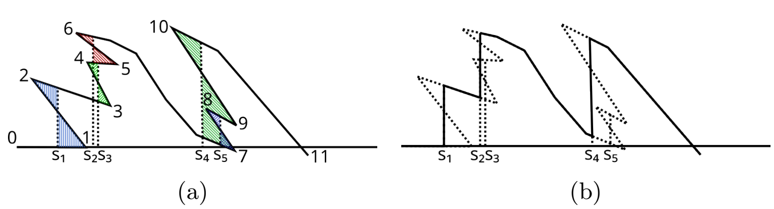

Fig. 3: Shockwave arrangement algorithm: a) placement of shockwaves according to the area balancing rule (equal areas are shaded with the same color); b) removal of overlapping shockwaves

ICCS Camera Ready Version 2025
To cite this paper please use the final published version:
DOI: 10.1007/978-3-031-97570-7_27

The area of the polygon cut off from the pressure distribution by the shock wave is calculated using the trapezoidal integration formula (Fig. 4), the shock wave AB is shown in green, the pressure distribution points are numbered 1-19.

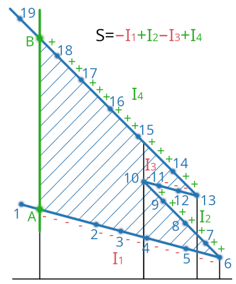

Fig. 4: An algorithm for calculating the area cut by a shock wave from a pressure distribution

An iterative algorithm is used to increase numerical stability. The new pressure distribution is calculated slightly away from the current height, instead of calculating immediately at the far field. This iterative process is repeated until the height reaches the far field.

3.2 Implementation in OpenFOAM

The algorithm described above is implemented as a library [21] based on the OpenFOAM software. The implemented library consists of a dynamic library containing far-field pressure calculation functions and a solver in which these functions are used. Due to this architecture, the user can use the solver directly or call the functions of the dynamic library in his own programs. For the solver, physical parameters are set by the user in the OpenFOAM dictionary, pressure signatures are read and written in CSV format. To speed up the computation, orientation points and areas under each segment of the linearly interpolated pressure distribution are cached in a dynamic array.

4 Numerical simulation of the sonic boom with OpenFOAM

The following approach is used to model the far-field sonic boom using OpenFOAM (Fig. 5). The near-field pressure at distances of the order of 1-5 model features is calculated using the rhoCentralFoam solver (Kurganov-Tadmor scheme) of the OpenFOAM package or dbnsFoam (HLLC scheme) of foam-extend. The pressure in the far field at distances of the order of 200-1000 model features is then determined from the obtained pressure distribution using the developed library.

ICCS Camera Ready Version 2025
To cite this paper please use the final published version:
DOI: 10.1007/978-3-031-97570-7_27

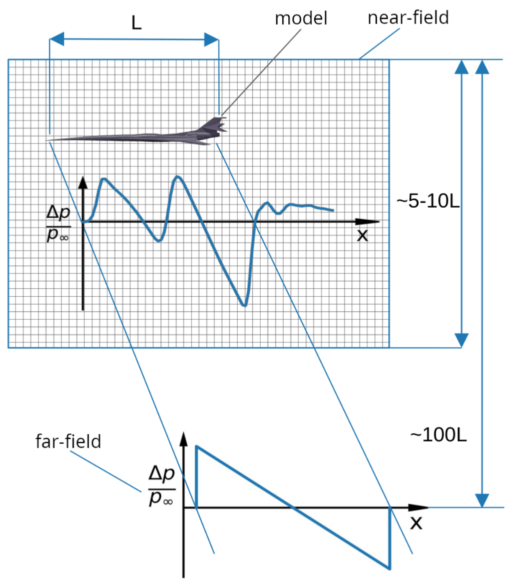

Fig. 5: A workflow for sonic boom prediction in OpenFOAM

Numerical simulations of the Seeb-ALR and 69°-delta wing models from the first NASA sonic boom workshop [9] and the c25d aircraft from the second [12] are performed. The results of the computation are compared with experimental data and the results of the workshop participants.

4.1 The Seeb-ALR model

The physical conditions at an altitude of 16 764 m similar to the experimental conditions are used in the simulation [9]: pressure of the upstream airflow $p_\infty =$ 9 183 Pa; sound velocity $c = 295$ m/s; temperature $T = 216.65$ K; Mach number $M = 1.6$. The turbulence model is not applied.

The model and fragments of the computational mesh are shown in Figure 6. The two-dimensional axisymmetric mesh is generated using the OpenFOAM utilities: snappyHexMesh and extrudeMesh. The characteristic size of the model is $L = 0.449$ m.

The rhoCentralFoam solver is used with the vanLeer interpolation scheme. The dbnsFoam solver is used with the HLLC scheme. The time step is chosen so that the Courant number is $Co = 0.3$. The comparison of the near-field pressure signatures to check the mesh convergence for different solvers is shown in Fig. 7. An additional comparison of these solvers on the same mesh showed that dbnsFoam completes the simulation significantly faster than rhoCentralFoam. For this reason, only dbnsFoam will be considered for further cases.

A comparison of dbnsFoam simulation results on the most detailed mesh with the experiment [9] is shown in Figure 8. A standard deviation is shown with a

ICCS Camera Ready Version 2025
To cite this paper please use the final published version:
DOI: 10.1007/978-3-031-97570-7_27

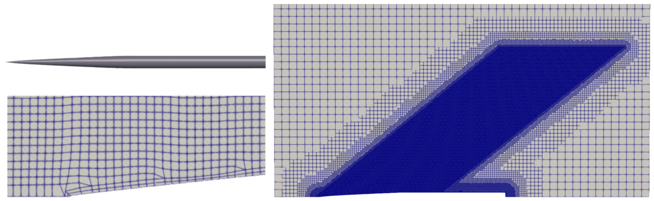

Fig. 6: The Seeb-ALR model and fragments of the computational mesh

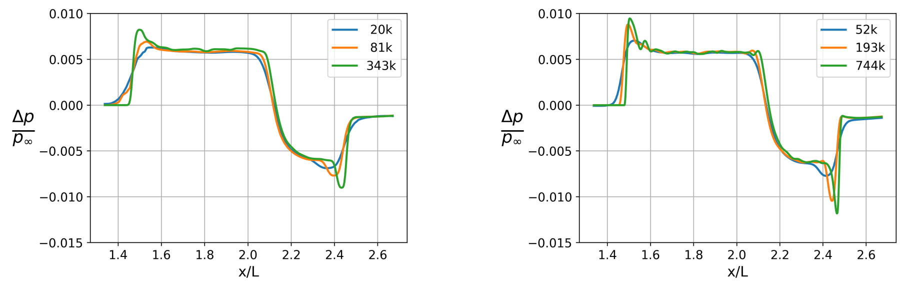

(a) (b)

Fig. 7: Comparison of near-field pressure signatures at distance $H/L = 1.2$ to check mesh convergence for the Seeb-ALR: a) rhoCentralFoam with vanLeer scheme; b) dbnsFoam with HLLC scheme

shaded area. It can be seen that the positions of the shocks are in good agreement with the experiment and the pressure level of the first two peaks and in the flattop region are within one standard deviation of the experiment. The simulation tends to give sharper shocks than the experiment, although two front shocks are within one standard deviation of the experiment, the rear shock is quite lower than in the experiment. As stated in [22], these discrepancies are observed because the peaks in the experiment are rounded due to the measurement approach. The simulation gives lower pressure in the tail region than in the experiment, the same result was observed by the workshop participants [10].Several theories were proposed and discussed in the paper [7] to explain this difference.

4.2 The 69°-delta wing model

The physical conditions used in the numerical simulation are similar to the experimental ones [9]: upstream pressure $p_\infty = 9\ 183$ Pa; sound velocity $c = 295$ m/s; temperature $T = 216.65$ K; Mach number $M = 1.7$; dynamic viscosity $\mu = 5.34 \cdot 10^{-6}$ Pa $\cdot$ s. The characteristic size of the model is $L = 0.175$ m.

The geometric model and fragments of the computational mesh are shown in Figure 9. The numerical simulation is performed with the fixture used in the aerodynamic experiment. Standard meshes proposed in the first NASA sonic

ICCS Camera Ready Version 2025
To cite this paper please use the final published version:
DOI: 10.1007/978-3-031-97570-7_27

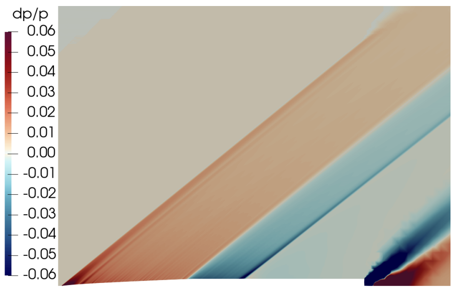

(a)

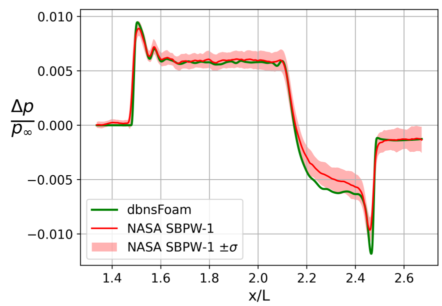

(b)

Fig. 8: Near-field simulation results for Seeb-ALR: a) pressure field; b) pressure signature comparison with experimental data at distance $H/L = 1.2$

boom workshop[9] are used. The number of cells in the most detailed mesh is 11.5 million.

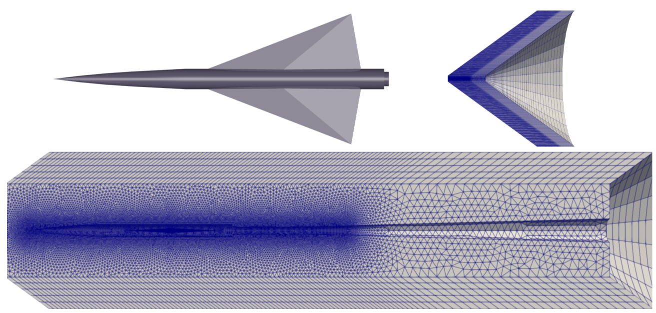

Fig. 9: The 69°-delta wing model and computational grid fragments

Numerical simulations are performed using the dbnsFoam solver with the HLLC scheme. The Courant number is set to $Co = 0.3$ and calculations are performed until steady state is reached. The near-field pressure field is shown in the figure 10a. Mesh convergence (Fig. 10b) is performed for meshes of 2.8, 5.9 and 11.5 million cells.

The comparison of the simulation results with the experiment[9] for the angle $\varphi = 0°$ is shown in the figures: for $r/L = 3.6$ (Fig. 11a), for $r/L = 4.6$ (Fig. 11b). The plots show that the amplitude of the second shock wave exceeds the experimental values, but similar behaviour is observed in the results of the SBPW-1 [10].

ICCS Camera Ready Version 2025
To cite this paper please use the final published version:
DOI: 10.1007/978-3-031-97570-7_27

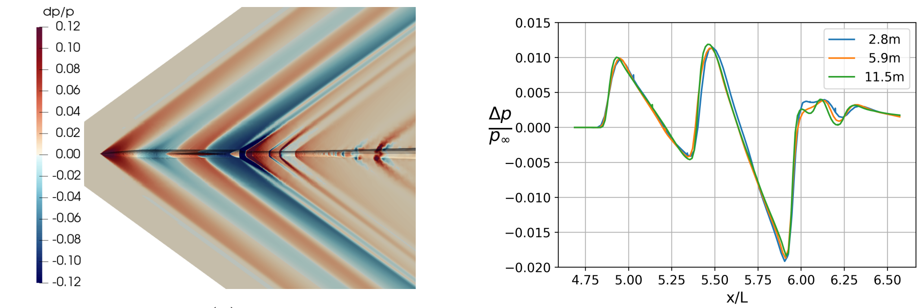

(a) (b)

Fig. 10: Near-field simulation results for 69°-delta wing model: a) pressure field; b) mesh convergence check, $r/L = 3.6$, angle $\varphi = 0°$

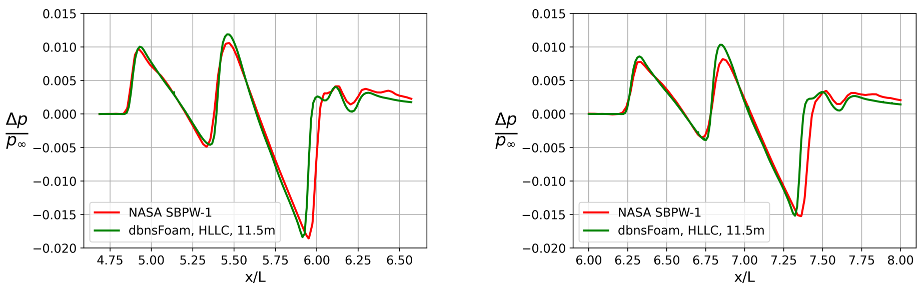

(a) (b)

Fig. 11: Comparison with experimental data for the pressure distribution angle $\varphi = 0°$ at distance: a) $r/L = 3.6$; b) $r/L = 4.6$

4.3 The c25d aircraft model

The physical conditions used in the numerical simulation are similar to the experimental ones [12]: upstream pressure $p_\infty = 10\ 682$ Pa; sound speed $c = 295$ m/s; temperature $T = 216.65$ K; Mach number $M = 1.6$; dynamic viscosity $\mu = 14.23 \cdot 10^{-6}$ Pa $\cdot$ s. The characteristic size of the model is $L = 32.92$ m.

The geometric model and fragments of the computational mesh are shown in Figure 12. The simulation does not take into account the presence of the engine, i.e. a flow configuration is used. The mesh proposed by the workshop [12] is used for this calculation. The number of cells in the mesh is 10.4 million. The calculation is performed using the dbnsFoam solver with Courant number $Co = 0.5$.

The near-field pressure field is shown in the figure 13. A comparison of the simulation results with those of the workshop participant [12] for the angle $\varphi = 0°$ for $r/L = 1$ is shown in figure 14. It can be seen that the result of the numerical simulation qualitatively reproduces all the main features of the flow.

ICCS Camera Ready Version 2025
To cite this paper please use the final published version:
DOI: 10.1007/978-3-031-97570-7_27

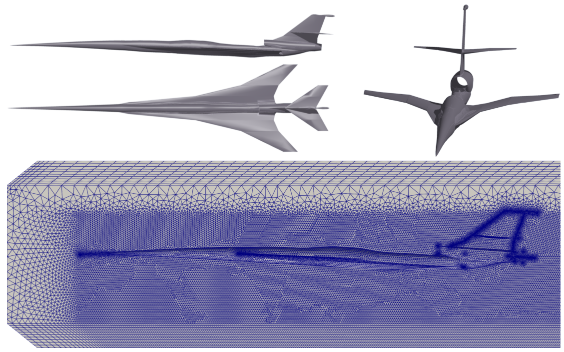

Fig. 12: The c25d aircraft model and computational grid fragment

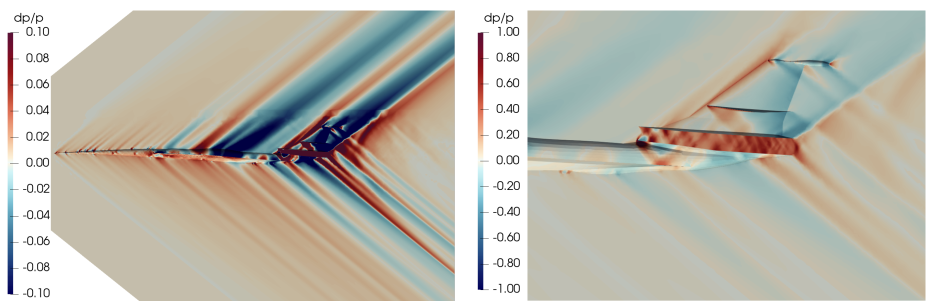

Fig. 13: Near-field pressure for flow around the c25d aircraft model

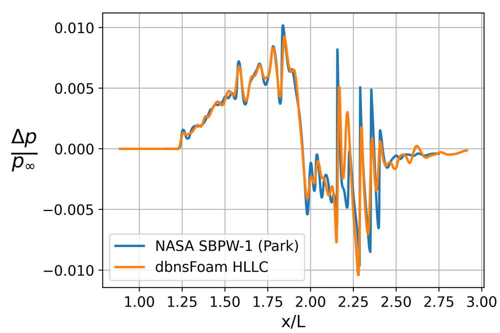

Fig. 14: Comparison of near-field pressure with experiment at $r/L = 1$, $\varphi = 0°$

4.4 Validation of numerical algorithm for far-field sonic boom prediction

The far-field pressure distribution is calculated using the proposed numerical algorithm and the results of the near-field numerical modeling of OpenFOAM as input data. In all cases, the most detailed grid is used. The far field sonic

ICCS Camera Ready Version 2025
To cite this paper please use the final published version:
DOI: 10.1007/978-3-031-97570-7_27

boom for Seeb-ALR is calculated at a distance of $r/L = 224$, for 69°-delta-wing at $r/L = 622$, for c25d at $r/L = 479$.

The figure 15 shows the comparison of the far-field calculation results with the results of the NASA workshop participants [9, 12] for models: Seeb-ALR (a), 69°-delta-wing (b), c25d (c). The abscissa is the characteristic time obtained by dividing the coordinate by the aircraft speed. In the workshop, the ground reflection factor K_g was 1.9, which means a single reflection of the shock waves from the ground.

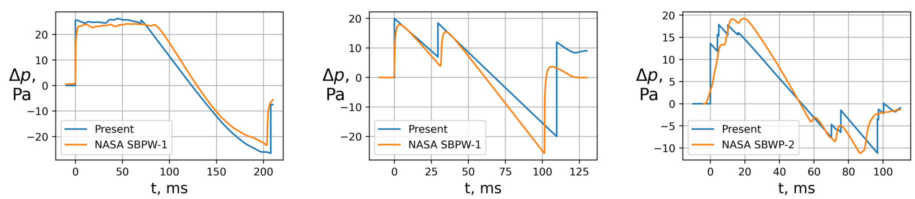

(a) (b) (c)

Fig. 15: Far-field pressure distributions for: a) Seeb-ALR; b) 69°-delta wing; c) c25d model

Conclusion

An open-source OpenFOAM library is developed to compute the far-field sonic boom pressure using the quasi-linear Whitham theory. Numerical simulations of the flow field around the Seeb-ALR, 69°-delta wing, c25d aircraft models presented at SBPW-1 and SBPW-2 are performed using the rhoCentraFoam and dbnsFoam solvers. Flow structures and near-field pressure distributions are obtained. Comparison of the near-field pressure distributions with experimental data and simulation results from NASA workshop participants shows good agreement. Based on the results, computational cases for these models have been prepared in OpenFOAM. These cases can be further used for validation in other investigations. The results of the near-field simulation in OpenFOAM are used to calculate and validate the developed numerical algorithm for the far-field sonic boom prediction.In general, the far-field pressures for all models under consideration are in good agreement with the benchmark data. The developed library and calculation cases are available on github [21].

References

1. Openfoam. https://www.openfoam.com/, access 23.12.2024

ICCS Camera Ready Version 2025
To cite this paper please use the final published version:
DOI: 10.1007/978-3-031-97570-7_27

2. Bashkirov, I., Chernyshev, S., Kazhan, A., Kazhan, V., Karpov, E., Shanygin, A., Shenkin, A.: Goals, tasks and technic concept of russian flight civil supersonic jet technology demonstrator. IOP Conference Series: Materials Science and Engineering **1226**(1), 012098 (2022). https://doi.org/10.1088/1757-899X/1226/1/012098
3. Bonavolontà, G., Lawson, C., Riaz, A.: Review of sonic boom prediction and reduction methods for next generation of supersonic aircraft. Aerospace **10**(11) (2023). https://doi.org/10.3390/aerospace10110917
4. Chernyshev, S., Gorbovskoy, V., Kazhan, , Korunov, : Re-entry vehicle sonic boom issue: Modelling and calculation results in windy atmosphere based on the augmented burgers equation. Acta Astronautica **194**, 450–460 (2022). https://doi.org/10.1016/j.actaastro.2021.12.038
5. Clarkson, B.L., Mayes, W.H.: Sonic-boom-induced building structure responses including damage. The Journal of the Acoustical Society of America **51**(2C), 742–757 (02 1972). https://doi.org/10.1121/1.1912907
6. Hicks, R.M., Mendoza, J.P.: Prediction of aircraft sonic boom characteristics from experimental near field results. Tech. Rep. NASA-TM-X-1477 (1967)
7. Housman, J.A., Sozer, E., Kiris, C.C.: LAVA Simulations for the First AIAA Sonic Boom Prediction Workshop. https://doi.org/10.2514/6.2014-2008
8. Kovalenko, V.V., Zhilin, Y.L.: On matching sonic boom near-field and far-field solutions. The Journal of the Acoustical Society of America **104**(3), 1831–1831 (1998). https://doi.org/10.1121/1.423495
9. Park, M.A., Morgenstern, J.M.: Summary and statistical analysis of the first aiaa sonic boom prediction workshop . https://doi.org/10.2514/6.2014-2006
10. Park, M.A., Morgenstern, J.M.: Summary and Statistical Analysis of the First AIAA Sonic Boom Prediction Workshop. https://doi.org/10.2514/6.2014-2006
11. Park, M.A., Carter, M.B.: Nearfield summary and analysis of the third aiaa sonic boom prediction workshop c608 low boom demonstrator. AIAA Scitech 2021 Forum (2020), https://api.semanticscholar.org/CorpusID:234273306
12. Park, M.A., Nemec, M.: Nearfield summary and statistical analysis of the second aiaa sonic boom prediction workshop. Journal of Aircraft (2017), https://api.semanticscholar.org/CorpusID:116283568
13. Pierce, A.D., Thomas, C.L.: Atmospheric correction factor for sonic-boom pressure amplitudes. The Journal of the Acoustical Society of America **46**(5B), 1366–1380 (11 1969). https://doi.org/10.1121/1.1911861
14. Plotkin, K.J.: Pcboom3 sonic boom prediction model, version 1.0e. Tech. Rep. Wyle Research Report WR 95-22E (10 1998)
15. Plotkin, K.J.: State of the art of sonic boom modeling. The Journal of the Acoustical Society of America **111**(1), 530–536 (2002). https://doi.org/10.1121/1.1379075
16. Qiao, J.L., Han, Z., Song, W., Song, B.F.: Development of Sonic Boom Prediction Code for Supersonic Transports Based on Augmented Burgers Equation. https://doi.org/10.2514/6.2019-3571
17. Rallabhandi, S.K.: Advanced sonic boom prediction using the augmented burgers equation. Journal of Aircraft **48**(4), 1245–1253 (2011). https://doi.org/10.2514/1.C031248
18. Stevens, S.S.: Perceived level of noise by mark vii and decibels (e). Journal of the Acoustical Society of America **51**, 575–601 (1972), https://api.semanticscholar.org/CorpusID:122297914
19. Sutherland, L., Czech, J.: Evaluation of human response to structural vibrations induced by sonic booms. Tech. Rep. NASA Contractor report 189584 (6 1992)
20. Thomas, C.: Eextrapolation of sonic boom pressure signatures by the waveform parameter method. Tech. Rep. NASA technical note TN D-6832 (7 1972)

ICCS Camera Ready Version 2025
To cite this paper please use the final published version:
DOI: 10.1007/978-3-031-97570-7_27

21. libSonicBoom, https://github.com/unicfdlab/libSonicBoom , online; accessed 28 Febrary 2025
22. West, T., Reuter, B., Walker, E., Kleb, W.L., Park, M.A.: Uncertainty Quantification and Certification Prediction of Low-Boom Supersonic Aircraft Configurations. https://doi.org/10.2514/6.2014-2139, https://arc.aiaa.org/doi/abs/10.2514/6.2014-2139
23. Whitham, G.B.: The behaviour of supersonic flow past a body of revolution, far from the axis. Proceedings of the Royal Society of London. Series A. Mathematical and Physical Sciences **201**, 109 – 89 (1950)
24. Whitham, G.B.: The flow pattern of a supersonic projectile. Communications on Pure and Applied Mathematics **5**(3), 301–348 (1952). https://doi.org/10.1002/cpa.3160050305
25. Yamashita, R., Nikiforakis, N.: Three-dimensional full-field simulation of sonic boom emanating from complex geometries over buildings. Shock Waves **33**, 149–167 (2023). https://doi.org/10.1007/s00193-023-01125-6
26. Zhilin, Y.L.: On sonic boom. Uch. Zap. TsAGI **2**(3), 1–11 (1971)

ICCS Camera Ready Version 2025
To cite this paper please use the final published version:
DOI: 10.1007/978-3-031-97570-7_27